POLITECNICO DI TORINO
Repository ISTITUZIONALE

Enhanced photocatalytic performance of LaFeO3/g-C3N4 heterojunctions for the degradation of orange G dye under visible light

Original
Enhanced photocatalytic performance of LaFeO3/g-C3N4 heterojunctions for the degradation of orange G dye under visible light / Baleh, H., Chakour, N., Djakhdane, K., Bassaid, S., Dehbi, A., Ouldhamadouche, N., Freyria, F.S., Bonelli, B., Coha, M., Ditaranto, N., Alsalme, A.. - In: RSC ADVANCES. - ISSN 2046-2069. - (2026). [10.1039/D6RA02138G]

Availability:
This version is available at: 11583/3014800 since: 2026-08-24T11:06:43Z

Publisher:
Royal Society of Chemistry

Published
DOI:10.1039/D6RA02138G

Terms of use:

This article is made available under terms and conditions as specified in the corresponding bibliographic description in the repository

Publisher copyright

(Article begins on next page)

18 November 2026

RSC Advances

PAPER

Published on 31 July 2026
Licensed under CC-BY-NC 4.0

Check for updates

Cite this: DOI: 10.1039/d6ra02138g

Enhanced photocatalytic performance of $LaFeO_3$/g-C_3N_4 heterojunctions for the degradation of orange G dye under visible light

Hinane Baleh,[a] Naziha Chakour,[a] Khaled Djakhdane,[a] Salah Bassaid,[a] Abdelkader Dehbi,*[a] Nadir Ouldhamadouche,[a] Francesca S. Freyria,*[b] Barbara Bonelli,[b] Marco Coha,[c] Nicoletta Ditaranto[d] and Ali Alsalme[e]

In this study, $LaFeO_3$/g-C_3N_4 (LFO/g-CN) hybrid materials with mass ratios of LFO and g-CN of 1/0.5, 1/1, and 1/1.5 were synthesized and evaluated for the visible light photocatalytic degradation of the azo-dye Orange G (OG). The composite materials were characterized to determine their textural, morphological, and optical properties. Preliminary photocatalytic results highlighted a significant synergistic interaction between LFO and g-CN. The LFO/g-CN (1/1.5) composite exhibits the highest activity, achieving 50% OG removal, representing a 2.7-fold improvement over pristine g-CN, with a rate constant of 0.0048 min^{-1} (3.7 times higher than bare g-CN). The degradation kinetics follow a pseudo-first-order model. The influence of key operational parameters, including catalyst loading, initial pH, pollutant concentration, and visible-light intensity, was systematically investigated using the optimized LFO/g-CN (1/1.5) composite. Optimal OG conditions (0.5 g L^{-1} catalyst, pH 2.0, 10 mg L^{-1} OG concentration, 0.95 W cm^{-2} visible light intensity) yielded a maximum rate constant of 0.0119 min^{-1} and 82% OG decolorization after 135 min. At higher catalyst or dye concentrations, the photocatalytic activity declined due to light scattering and surface saturation. Enhanced OG degradation under acidic conditions was attributed to favourable electrostatic attraction between the positively charged catalyst surface and anionic OG moieties. The composite also demonstrated excellent stability, retaining over 77% of its initial activity after four reuse cycles. These findings highlight the potential of LFO/g-CN heterojunctions as efficient visible-light photocatalysts for sustainable water remediation.

Received 13th March 2026
Accepted 10th July 2026

DOI: 10.1039/d6ra02138g

rsc.li/rsc-advances

Introduction

Environmental contamination resulting from industrial activities has become a significant challenge facing modern society. The release of toxic compounds, particularly synthetic dyes, into water systems represents an important environmental risk due to their chemical stability, non-biodegradability, and potential toxicity to living organisms. Conventional water treatment methods are often ineffective at completely removing such pollutants, which has encouraged the development of advanced oxidation processes (AOPs), such as photocatalysis.[1,2]

Photocatalysis using semiconductor materials has attracted increasing attention as an efficient and sustainable method for degrading organic contaminants under irradiation.[3,4] Under light excitation, semiconductor catalysts generate reactive oxygen species, including hydroxyl and superoxide radicals ($OH^{\bullet}$, $O_2^{-\bullet}$), which drive oxidation of organic compounds.[5,6] Early research in this field primarily used UV-active semiconductors such as TiO_2 and ZnO; however, the limited fraction of UV light in the solar spectrum (less than 5%) limits their efficiency.[7] Consequently, other research efforts are focused on developing visible light-responsive photocatalysts that can operate efficiently under mild illumination conditions.[8–10]

Among visible-light-driven semiconductors, polymeric graphitic carbon nitride (g-C_3N_4) has attracted substantial interest owing to its metal-free composition, chemical and thermal stability, and ease of synthesis from inexpensive precursors such as urea or melamine.[11–13] With a band gap of approximately 2.7 eV, g-C_3N_4 (g-CN) can be excited by visible light up to 460 nm, making it a promising material for photocatalytic degradation of organic pollutants, hydrogen evolution, and CO_2 reduction. Nonetheless, the photocatalytic performance of pristine g-C_3N_4 is significantly hindered by its low

[a]Engineering Physics Laboratory, Faculty of Material Sciences, University of Tiaret, Tiaret, 14000, Algeria. E-mail: abdelkader.dehbi@univ-tiaret.dz

[b]Department of Applied Science and Technology (DISAT), Politecnico di Torino, and INSTM Unit of Torino – Politecnico, Corso Duca degli Abruzzi 24, 10129 Torino, Italy. E-mail: francesca.freyria@polito.it

[c]Department of Environment, Land and Infrastructure Engineering (DIATI) & Clean Water Center (CWC) – Politecnico di Torino, Corso Duca degli Abruzzi 24, 10129 Torino, Italy

[d]Department of Chemistry, Università degli Studi di Bari Aldo Moro, 70125 Bari, Italy

[e]Department of Chemistry, College of Science, King Saud University, Riyadh 11451, Saudi Arabia

© 2026 The Author(s). Published by the Royal Society of Chemistry

surface area and rapid recombination of photogenerated charge carriers, resulting in reduced photocatalytic efficiency. To overcome these drawbacks, several modification strategies, such as heteroatom doping, morphological control, and heterojunctions formation with other semiconductors, have been proposed.[14,15]

The coupling of g-C_3N_4 with other semiconductors, like TiO_2, ZnO, and Bi_2WO_6, has been shown to enhance photocatalytic performance. These hybrid systems exhibit improved charge separation efficiency, broader light absorption, and higher surface reactivity.[16–18]

In this context, the perovskite-type oxide lanthanum ferrite ($LaFeO_3$, LFO) stands out as an auspicious material due to its narrow band gap (1.8–2.1 eV), strong visible light absorption, and robust structural and chemical stability. Structurally, $LaFeO_3$ possesses an orthorhombic perovskite framework composed of corner-sharing FeO_6 octahedra, with La^{3+} ions occupying interstitial sites.[19] Its excellent redox activity and tuneable electronic structure have led to wide application in sensors,[20] supercapacitors,[21] photocatalysis,[22] and solid oxide fuel cells.[23] Given its narrow band gap and strong visible light absorption, according to the literature coupling $LaFeO_3$ with g-C_3N_4 is an effective strategy to form heterojunctions that facilitate charge transfer across interfaces, suppress electron/hole recombination, and extend light absorption into the visible region.[24–27] Several studies confirmed that $LaFeO_3$/g-C_3N_4 heterojunctions exhibit markedly enhanced photocatalytic performance compared with the individual components. This improvement is attributed to efficient interfacial charge separation and the synergistic interaction between the perovskite and carbon nitride phases.[28,29]

Beyond $LaFeO_3$/g-C_3N_4 systems, several other perovskite/g-C_3N_4 heterostructures have been reported to exhibit promising photocatalytic activity. For instance, $LaCoO_3$/g-C_3N_4 and $LaNiO_3$/g-C_3N_4 composites have shown enhanced degradation of dyes and antibiotics under visible light, attributed to effective interfacial charge transfer and strong visible-light absorption.[30,31] Similarly, coupling g-C_3N_4 with other transition-metal compounds, such as FeO_x and FeS_2, has demonstrated improved pollutant removal efficiencies due to synergistic effects between wide-bandgap oxides/sulphides and g-C_3N_4.[32,33] Recently, ternary architectures, such as α-Fe_2O_3/g-C_3N_4/Fe_3O_4 and TiO_2/g-C_3N_4/WS_2, have further highlighted the benefits of combining multiple semiconductors for improved light harvesting and charge separation.[34,35] Overall, these studies highlight the importance of combining complementary semiconductors to enhance photocatalytic efficiency for environmental remediation. More broadly, recent advances in heterostructured and two-dimensional materials, including MXenes and sulfide-based systems, further confirm the importance of interfacial engineering for improving charge transport and catalytic performance in energy and environmental applications.[36]

In our recent work,[37] we synthesized a composite of $LaFeO_3$ and g-C_3N_4 (LFO/g-CN) *via* a wet impregnation method and evaluated its performance in the adsorption removal of Orange G (OG), a typical azo dye and water pollutant, from aqueous solution. The introduction of g-CN significantly increased the LFO material's specific surface area (from 3.7 $m^2\ g^{-1}$ for LFO alone to 51 $m^2\ g^{-1}$ for the composite) and improved the textural and surface properties of the adsorbent. The previous study demonstrated a promising route to combine the physico-chemical advantages of perovskite-type $LaFeO_3$ with g-C_3N_4 to produce a robust adsorbent for dye remediation in aqueous systems.[37]

In the present study, we extend this approach by investigating the photocatalytic performance of LFO/g-CN. Here, the composites with different $LaFeO_3$/g-C_3N_4 mass ratios were synthesized using the same wet impregnation strategy and evaluated for the visible-light-driven degradation of OG. Pristine g-CN was prepared by thermal polymerization of urea, while LFO was synthesized through a sol–gel route followed by calcination at 700 °C.

The resulting composite materials were characterized by various physico-chemical techniques, namely: X-ray powder diffraction, porosimetry and surface area analysis, field emission scanning microscopy coupled to energy dispersive spectroscopy, diffuse reflectance UV-Vis spectroscopy, X-ray photoelectron spectroscopy and photoluminescence spectroscopy to determine the textural, morphological, and optical properties of the samples.

The composite with an LFO/g-CN mass ratio of 1/1.5 exhibited the highest degradation rate constant under visible-light irradiation. Therefore, this formulation was selected for a more detailed study. Its photocatalytic performance was further investigated by varying several operational parameters, including catalyst loading, solution pH, pollutant initial concentration, and visible-light intensity, to identify the parameters governing photocatalytic efficiency. In addition, radical scavenger experiments were performed to identify the main reactive species involved in OG degradation, while high-performance liquid chromatography – mass spectrometry and UV-Vis analyses were carried out to monitor the disappearance of the parent dye and the formation of transformation products, providing further insight into the reaction pathway. The reusability and stability of the optimized photocatalyst were also assessed to examine its potential for practical wastewater treatment applications.

Materials and methods

Chemicals

Lanthanum nitrate hexahydrate, $La(NO_3)_3 \cdot 6H_2O$, was purchased from LOBA CHEMIEPVP. LDT. Urea, CH_4NO_2, polyvinylpyrrolidone (K-30), iron(III) nitrate nonahydrate, $Fe(NO_3)_3 \cdot 9H_2O$, and orange G dye ($C_{16}H_{10}N_2Na_2O_7S_2$, OG) were procured from BIOCHEM Chemopharma, *N*,*N*-dimethylformamide from ANALAR Normapur, and methanol from GPR Rectapur. Ethylene diamine tetra acetic acid (EDTA, 99%), isopropanol (IPA, 98%), and benzoquinone (BQ, ≥98%), which were used as scavenger agents, were purchased from Biochem Chemopharma and Sigma-Aldrich.

© 2026 The Author(s). Published by the Royal Society of Chemistry

Synthesis of g-CN, LFO, and LFO/g-CN composites

The graphitic carbon nitride powder was synthesized by direct thermal polymerization of urea, as previously reported.[38] Specifically, 10 g of urea was placed in a covered porcelain crucible and heated up to 520 °C (heating rate = 10 °C min^{-1}) in a muffle furnace, where the final temperature was maintained for 4 h. After natural cooling, the resulting yellow product was ground into a fine powder.

The perovskite-type LFO was prepared *via* the sol–gel route using $La(NO_3)_3 \cdot 6H_2O$ and $Fe(NO_3)_3 \cdot 9H_2O$ as metal precursors dissolved in 50 mL *N*,*N*-dimethylformamide. After 1 h of stirring, 0.9 g polyvinylpyrrolidone (K-30) was added as a stabilizing agent, and the mixture was heated to form a viscous gel. The obtained gel was then calcined in air at 700 °C for 3 h (heating rate = 5 °C min^{-1}) to yield the perovskite phase.[39]

The LFO/g-CN composites were synthesized by thermal wet impregnation: the desired proportions of LFO and g-CN (1/0.5, 1/1, and 1/1.5 by mass) were dispersed in 40 mL of methanol, sonicated for 1 h, and stirred at 60 °C for 24 h. The resulting suspensions were filtered and dried at room temperature to obtain the composite photocatalysts.[37]

Characterization methods

X-ray diffraction (XRD) patterns were collected on the powder samples using an X'Pert Philips PW3040 diffractometer with Cu Kα radiation (2θ range = 10°–80°; step = 0.026° 2θ). The XRD patterns were indexed using the Powder Diffraction File (PDF 2000, 2004, International Centre for Diffraction Data, Pennsylvania).

N_2 adsorption/desorption isotherms were measured at −196 °C using a Micromeritics ASAP 2020Plus instrument. Before analysis, powders were pre-outgassed at 150 °C for 4 h to remove water and other atmospheric contaminants. The Specific Surface Area (SSA) was calculated using the Brunauer–Emmett–Teller (BET) method.

FE-SEM (field emission scanning electron microscopy) micrographs of the powders were taken on a Merlin FE-SEM instrument (Zeiss). Elemental analysis was performed by acquiring at least 2 Energy-Dispersive Spectroscopy (EDS) maps and corresponding spectra for each sample using an Oxford X-ray EDS detector, enabling qualitative assessment of the chemical composition. Particle size distribution was determined using ImageJ software by analysing five different FE-SEM micrographs and measuring at least 100 particles.

Diffuse Reflectance (DR) UV-Vis spectra of the materials were measured using a Cary 5000 UV-Vis-NIR spectrophotometer (Varian Instruments) equipped with a DR sphere for analysis of powders. The surface chemical composition, speciation and valence band determination were analysed using X-ray photoelectron spectroscopy (XPS) with a Versa Probe II scanning XPS microprobe spectrometer (Physical Electronics GmbH), equipped with a monochromatized Al Kα source (X-ray spot = 200 μm) at a power of 24.8 W. Both wide scans and high-resolution XP spectra were obtained using a fixed analyser transmission (FAT) mode with pass energies of 117.40 eV and 46.95 eV, respectively. An electron gun facilitated charge compensation (1.0 V, 20.0 μA). All the binding energy (BE) values were referenced to the C1s line at 284.8 ± 0.1 eV for adventitious carbon. Data processing was completed using MultiPak software version 9.9.0.8. Photoluminescence (PL) spectra were collected using a PerkinElmer LS55 spectrofluorometer equipped with a powder sample holder.

Photocatalytic activity experiments

Photocatalytic degradation experiments were performed in a double-walled reactor, irradiated under visible light using four 75 W OSRAM lamps (400–700 nm) positioned symmetrically around the reactor. The irradiation time was fixed at 135 min. The operating temperature was maintained at 25 °C by continuous water circulation. Pristine LFO, pristine g-CN, and LFO/g-CN composite photocatalysts with different mass ratios of LFO and g-CN (LFO/g-CN equal to 1/0.5, 1/1, 1/1.5) were dispersed in 100 mL of an aqueous orange G (OG) solution (10 mg L^{-1}) under magnetic stirring and ambient air conditions. OG, an anionic dye, was employed as a model pollutant; its molecular structure and UV-vis absorption spectrum in distilled water are shown in Fig. 1. Before light irradiation, the suspensions were sonicated for 5 min to ensure homogeneous catalyst dispersion and subsequently stirred in the dark for 60 min to establish adsorption–desorption equilibrium. During photocatalytic reactions, aliquots of 3 mL of OG solution were withdrawn at regular time intervals, filtered to remove photocatalyst particles, and analysed by a SHIMADZU UV-1650PC UV-Vis spectrophotometer at 478 nm (maximum absorption wavelength). The decrease in the intensity of this chromophore absorption band was used to evaluate the percentage of OG decolorization.

To study the role of reactive species in the photocatalytic degradation of OG by the LFO/g-CN (1/1.5) composite under visible light, experiments were conducted with selected scavengers. EDTA was used to scavenge photogenerated holes (h^+), isopropanol (IPA) as a hydroxyl radical scavenger ($OH^\bullet$), and benzoquinone (BQ) to scavenge superoxide radicals ($O_2^{-\bullet}$). Each

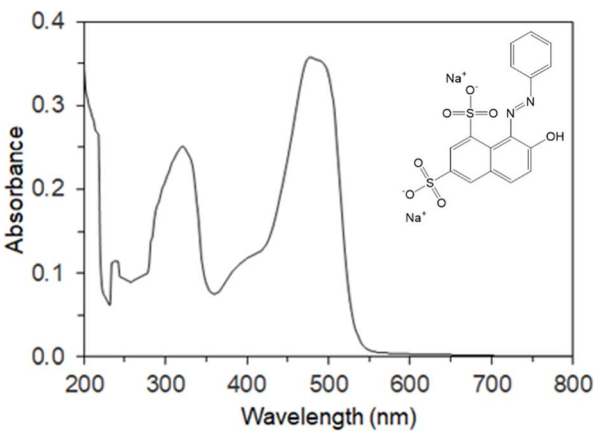


Fig. 1 UV-Vis absorption spectrum of the aqueous OG solution used for the photocatalytic tests. The OG molecular structure is reported on the top right corner.

© 2026 The Author(s). Published by the Royal Society of Chemistry

scavenger, with a concentration of 1 mmol L^{-1}, was added individually to the OG solution before irradiation, and the degradation was conducted under the same operating conditions as the usual photocatalytic tests.

Chromatographic analyses

The degradation of OG was monitored by reversed-phase high-performance liquid chromatography (RP-HPLC). The chromatographic analyses were performed using a Shimadzu Nexera Series 40 HPLC system equipped with an online degasser, a pump incorporating a low-pressure gradient mixer, an autosampler, a temperature-controlled column compartment, and a photodiode array (PDA) detector. Separation was achieved on a Restek Roc C18 analytical column (150 × 4.6 mm i.d., 5 μm particle size) fitted with an in-line guard filter to prevent contamination of the analytical column by particulate matter. The mobile phase consisted of acidified water (300 μL L^{-1} of 85% H_3PO_4; solvent A) and acetonitrile (solvent B). Elution was carried out at a flow rate of 1.0 mL min^{-1} using a linear gradient from 90 : 10 to 70 : 30 (A : B, v/v) over 10 min, followed by a linear increase to 100% B over the subsequent 5 min. The initial mobile phase composition was then restored, and the column was re-equilibrated, resulting in a total run time of 21 min. The injection volume was 10 μL. The column temperature was maintained at 40 °C, while the autosampler was kept at 5 °C. UV-Vis spectra were acquired in the 190–800 nm wavelength range to monitor the degradation process.

The possible formation of transformation products was investigated by ultra-high-performance liquid chromatography coupled with quadrupole time-of-flight mass spectrometry (UHPLC-QTOF-MS). Analyses were performed using a similar Shimadzu Nexera Series 40 UHPLC system coupled to a SCIEX X500R quadrupole time-of-flight (QTOF) mass spectrometer equipped with a TurboIonSpray electrospray ionization (ESI) source. Chromatographic separation was achieved on a Gemini C18 column (100 × 2.0 mm i.d., 3 μm particle size, 110 Å) using water (solvent A) and methanol (solvent B), both containing 5 mM ammonium formate, as the mobile phases. The flow rate was set at 0.30 mL min^{-1} and the injection volume was 10 μL. The chromatographic gradient was identical to that described for the HPLC-UV-Vis analyses. The column oven and autosampler were maintained at 40 and 5 °C, respectively.

The mass spectrometer was operated in both positive and negative ESI modes over an m/z range of 50–1400. The ion source temperature was maintained at 350 °C, and the ion spray voltage was set to +4.5 kV and −4.5 kV for positive and negative ionization modes, respectively. Data were acquired in information-dependent acquisition (IDA) mode. The collision energy (CE) was set at ±25 V (with a CE spread equal to 15 V) for TOF-MS/MS experiments. Up to ten precursor ions were selected during each acquisition cycle for MS/MS fragmentation and dynamic background subtraction was enabled.

Stability and reusability tests

The stability and reusability of the photocatalyst are crucial, particularly for practical applications. The recycling performance of the LFO/g-CN (1/1.5) composite was evaluated through successive photocatalytic degradation cycles. After each photocatalytic run, the catalyst was recovered from the OG solution, thoroughly washed several times with deionized water, centrifuged, and oven-dried before being reused in a fresh OG solution. Four consecutive photocatalytic cycles were conducted using the same catalyst batch. For each cycle, all the optimized experimental parameters, including catalyst dosage, OG solution volume, initial pH solution (2.0), temperature, initial OG concentration, light intensity, and distance from the light source, were carefully maintained to ensure consistent reaction conditions. After the recycling tests, XRD analysis, FE-SEM/EDS elemental mapping and XPS were performed on the recovered photocatalyst to assess possible structural, morphological, and compositional changes. In addition, ICP-MS analysis (inductively coupled plasma mass spectrometry) on an ICAP Q (Thermofisher) was carried out on the recovered powder. For this analysis, approximately 3 mg of sample were digested in 3 mL of concentrated HNO_3 by heating on a hot plate under a watch glass until complete dissolution. The resulting solution was then transferred into a 25 mL volumetric flask and diluted to volume with ultrapure water. Before ICP-MS analysis, the digested solution was further diluted by two successive dilution steps, 1 : 25 and 1 : 10. The diluted samples were analysed using a four-point external calibration curve prepared at 100, 500, 1000, and 2000 ppb.[40]

Results and discussion

Physico-chemical characterization of the samples

Fig. 2 reports the XRD patterns of the pristine g-CN (inset) and LFO, along with those of the three LFO/g-CN composites. The pristine LFO shows sharp peaks at 22.5 (101), 25.3 (111), 32.1 (121), 34.1 (210), 37.9 (112), 39.7 (220), 41.3 (131), 43.0 (221), 46.2 (202), 47.7 (212), 50.4 (132), 52.0 (103), 53.3 (311), 57.4 (123), 63.7 (331), 67.4 (242), 68.4 (410), 72.0 (143), 73.0 (313), 76.7 (204) and 77.6 (412) 2θ values (asterisks), due to the $LaFeO_3$ orthorhombic phase (JCPDS file:01-08-0641).

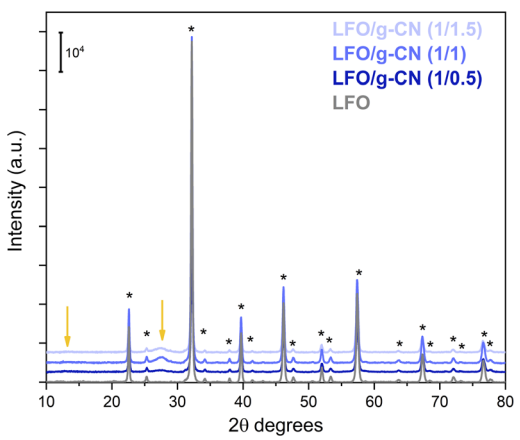


Fig. 2 XRD patterns of the pristine LFO and of the three LFO/g-CN composites in the 10–80 2θ degrees range; asterisks: peaks related to the $LaFeO_3$ phase; arrows: reflections of "disordered" g-C_3N_4 phase.

© 2026 The Author(s). Published by the Royal Society of Chemistry

Using the Williamson–Hall method applied to the fitted diffraction profiles, the average crystallite size is approximately 68 ± 10 nm, with no significant differences among the various LFO/g-CN composites. Compared to the pristine LFO, the three LFO/g-CN composites exhibit similar diffraction peaks characteristic of the $LaFeO_3$ phase. In addition, a broad feature with a maximum at approximately 27.3 2θ degrees (arrow in Fig. 2) is observed, whose intensity increases with the g-CN mass

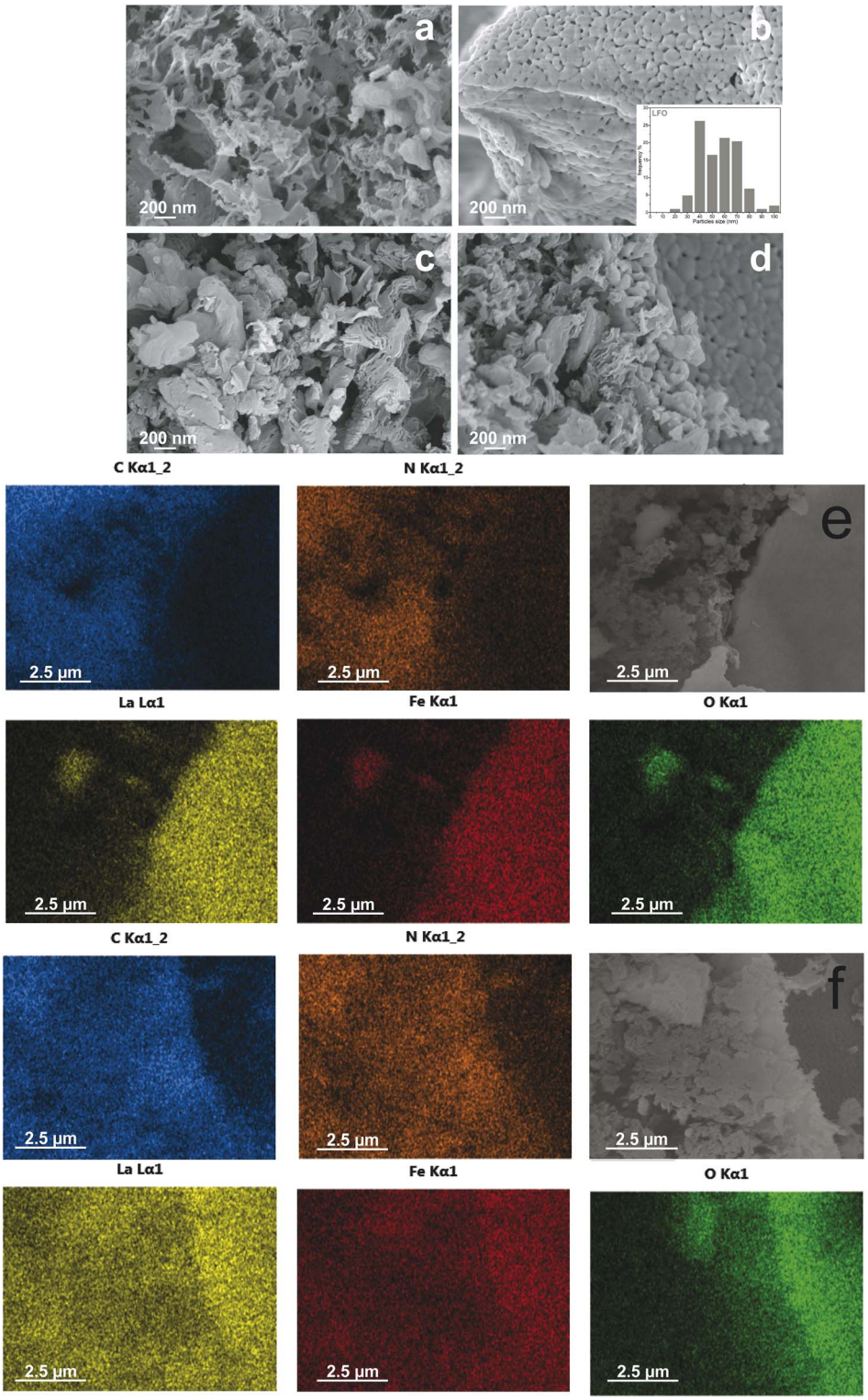


Fig. 3 Selected FE-SEM micrographs of (a) pristine g-CN (b) and LFO, inset (particle size distribution); LFO/g-CN (1/1.5) composite showing a g-CN-rich (c) region along with LFO/g-CN heterojunctions (d). The images' magnification was 100kx. Selected EDS elemental maps (e and f) of two distinct areas of the LFO/g-CN (1/1.5) composite.

© 2026 The Author(s). Published by the Royal Society of Chemistry

fraction. This signal is ascribed to the (002) reflection of g-C_3N_4, corresponding to the interlayer stacking of the C–N conjugated aromatic layers. At approximately 12.8° 2θ values, where the (100) or (210) reflections of g-C_3N_4 are expected, a slight rise in background intensity is observed, instead of a distinct peak. This phenomenon may be related to the formation of $LaFeO_3$/g-C_3N_4 composites, which corresponds to the disordering of the parent g-CN structure, supporting the idea that the employed synthesis procedure was successful.

Fig. 3 shows selected FE-SEM micrographs of the pristine g-CN and LFO (Fig. 3a and b, respectively) and of the LFO/g-CN (1/1.5) composite (Fig. 3c and d), which was chosen for the microscopic inspection due to its superior photocatalytic activity towards the OG degradation under visible light (*vide infra*). Fig. 3e and f show two selected EDS maps of the LFO/g-CN (1/1.5) composite. The pristine g-CN (Fig. 3a) occurs as flakes with a few nanometer-thick layers. The parent LFO shows the occurrence of highly aggregated/agglomerated nanoparticles with an average size of 60 nm ± 16 nm (inset to Fig. 3b) that is close to the average crystallite dimensions as determined by XRD.

The FE-SEM inspection of the LFO/g-CN (1/1.5) composite shows some heterogeneous regions, mostly g-CN-rich (Fig. 3c), along with LFO/g-CN heterojunctions (Fig. 3d). The occurrence of g-CN-rich regions is readily explained by considering that the two materials have different molar masses, and the LFO/g-CN mass ratio of 1/1.5 corresponds to an LFO/g-CN molar ratio of 0.34/1. Notwithstanding all this, heterojunctions are observed, as shown in the EDS elemental maps in Fig. 3e and f, where the spectra of the different elements are superimposed, confirming their formation.

Table 1 reports the values of the BET SSA of the composites and the pristine nanomaterials, as obtained by N_2 sorption isotherms, previously presented in ref. 37. The pristine LFO has an SSA of 3.7 $m^2\ g^{-1}$, whereas pure g-CN exhibits a significantly higher SSA of 37 $m^2\ g^{-1}$. The pristine LFO and the composites show Type II isotherms with an H3 hysteresis loop, typical of non-porous or macroporous adsorbents, in which capillary condensation occurs within slit-shaped pores, typically arising from aggregates/agglomerates of plate-like particles. The SSA increases markedly in the composites due to the presence of g-CN, reaching 51 $m^2\ g^{-1}$ for LFO/g-CN (1/1.5). To confirm this observation, the LFO/g-CN (1/1) composite was also analysed: it showed a Type 2 isotherm (not reported), a H3 hysteresis loop, and a slightly lower BET SSA of 44 $m^2\ g^{-1}$. As expected, the highest SSA is obtained with the composite containing the higher amount of g-CN, highlighting that this material positively affects (enhances) the SSA and the porosity of the composites. This fact could favour diffusion phenomena during photocatalytic processes within mesopores, allowing large molecules to approach active sites and reaction products to diffuse out of the photocatalyst's porous network.

Table 1 Values of BET SSA ($m^2\ g^{-1}$) and total pore volume ($cm^3\ g^{-1}$) as obtained by measuring the N_2 adsorption/desorption isotherms at −196 °C

Sample	BET SSA ($m^2\ g^{-1}$)	Total pore volume ($cm^3\ g^{-1}$)
LFO	3.7	0.012
g-CN	37	0.18
LFO/g-CN (1/1)	44	0.24
LFO/g-CN (1/1.5)	51	0.22

The optical properties of photocatalysts, including their absorption edge and defect-related electronic states, play a crucial role in determining photocatalytic performance, as they can influence light-harvesting ability and charge-carrier recombination processes. Fig. 4a reports the DR-UV-Vis spectra of the pristine g-CN[11] and LFO samples, along with

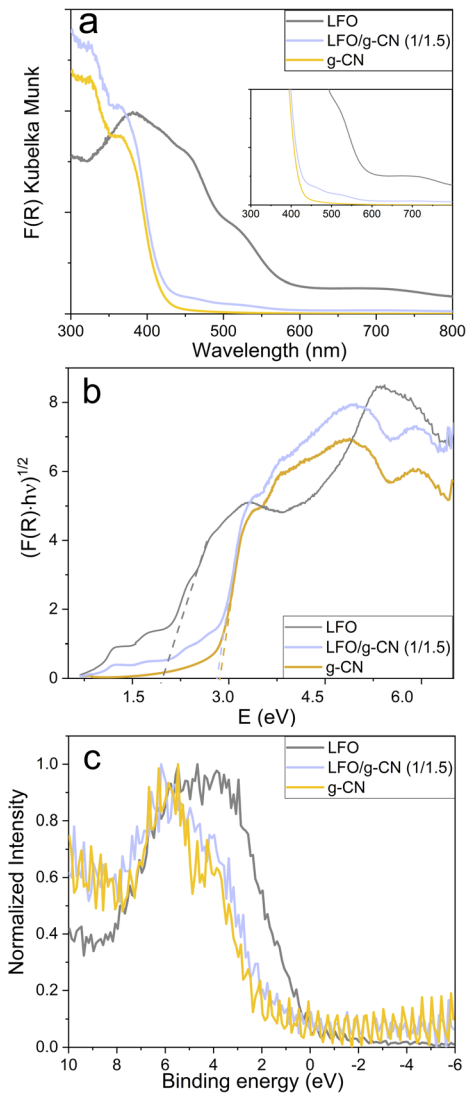


Fig. 4 (a) DR-UV-Vis spectra of the pristine LFO and g-CN, along with that of the LFO/g-CN (1/1.5) composite. The inset shows a magnification of the spectra, highlighting the presence of LFO-related absorption bands in the composites; (b) corresponding Tauc plots, as obtained by plotting $(F(R) \times h\nu)^{1/2}$ *vs.* $E(h\nu)$, assuming that both g-CN and LFO are indirect semiconductors. The dotted lines allow extrapolation of the semiconductor bandgap values; (c) XPS-determined valence band spectra of the three samples.

© 2026 The Author(s). Published by the Royal Society of Chemistry

that of the LFO/g-CN (1/1.5) composite in the 300–800 nm range. The DR UV-Vis spectrum of the pristine g-CN shows a broad absorption in the UV range due to the π–π* electron transition. A weaker tail extending into the visible region is also observed, and it is commonly attributed in the literature to n–π* electronic transitions, which can extend the absorption of g-C_3N_4 to approximately 600 nm, thereby enhancing its photocatalytic activity.[41]

The pristine LFO shows intense absorption in the UV and Vis regions, with a broad, intense band below 600 nm, due to ligand-to-metal charge-transfer (LMCT) transitions from O 2p to Fe 3d levels. The less intense absorption band at approximately 700 nm is commonly attributed to defect-related states and less probable charge-transfer processes, consistent with the fact that La ions do not significantly contribute to the formation of the fundamental band gap.[42,43]

The LFO/g-CN (1/1.5) composite shows a "hybrid" DR-UV-Vis spectrum, characterized by both a strong absorption below 425 nm, due to the g-CN related electronic transitions, and by a pronounced tail towards longer wavelengths (highlighted in the inset, Fig. 4a), due to the LFO-related electronic transitions. The DR-UV-Vis spectra of the other two composites, with LFO/g-CN mass ratios of 1/0.5 and 1/1, exhibit more intense LFO bands, consistent with their chemical compositions (not shown). To obtain a more accurate evaluation of the samples' band gaps, the Tauc plot method has been applied by plotting $(F(R) \times h\nu)^{1/2}$ *vs.* $h\nu$, assuming, in the first instance and according to most of the literature, that both g-CN and LFO are indirect semiconductors.[38,44] The corresponding curves are reported in Fig. 4b. The Tauc plot determined bandgap values of 2.85 and 1.98 eV for pristine g-CN and LFO, respectively, and 2.79 eV for the LFO/g-CN (1/1.5) composite. The composite shows only a slight redshift in the absorption edge compared to the g-CN, given its relatively low LFO/g-CN molar ratio (*vide supra*). All this notwithstanding, the presence of LFO gives rise to an extended absorption in the visible range, as expected. LFO positively affects the composites' optical properties, improving their absorption in the visible range and overcoming the optical limitations of g-CN. Valence-band XP spectra were collected to further investigate the surface electronic structure of pristine LFO, pristine g-CN, and the LFO/g-CN (1/1.5) heterojunction. As shown in Fig. 4c, the valence-band profile of the composite closely resembles that of pristine g-CN, indicating that its surface chemistry is dominated by g-CN. This result is consistent with the FE-SEM/EDS observations (Fig. 3), which showed the presence of g-CN-rich regions together with LFO/g-CN interfacial contact areas (Fig. 3c and d). The valence-band maxima, estimated from the linear extrapolation of the leading edge of the VB-XPS spectra, were located at −0.2 eV for LFO,[45] 0.90 eV for g-CN, and 0.7 eV for LFO/g-CN (1/1.5). The VB position of the composite is therefore closer to that of pristine g-CN, further confirming the dominant contribution of g-CN to the surface electronic structure of the heterojunction. The slight shift observed for the composite may be associated with electronic interaction between LFO and g-CN at the heterojunction interface.

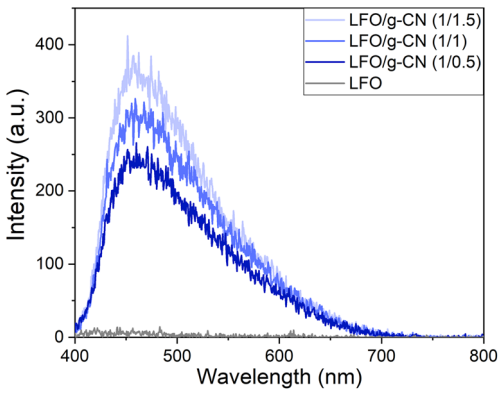


Fig. 5 Solid-state PL spectra of LFO and the LFO/g-CN composites excited at 300 nm.

Solid-state PL measurements were further performed to evaluate the radiative recombination features of the LFO/g-CN heterojunctions. As shown Fig. 5, the pristine LFO exhibits negligible emission under the adopted conditions, whereas all the LFO/g-CN samples display a broad visible emission band centred at approximately 460 nm. This band can be mainly attributed to g-CN-related radiative recombination, in agreement with literature reports on urea-derived g-C_3N_4 calcined at around 500–550 °C, where blue PL emission near 465 nm is commonly observed.[46,47] The PL intensity increases with increasing the g-CN content, following the order LFO/g-CN (1/1.5) > LFO/g-CN (1/1) > LFO/g-CN (1/0.5) >> LFO. The marked difference between pristine LFO and the composites confirms that the optical emission response of the heterojunctions is dominated by the g-CN phase and supports the occurrence of electronic/optical interaction between the two semiconductors.

Photocatalytic degradation of OG dye

Preliminary photocatalytic tests. Fig. 6a depicts the adsorption behaviour and visible light photocatalytic degradation of OG over LFO, g-CN, and various LFO/g-CN heterojunctions with different mass ratios. The photocatalyst concentration, solution pH, and the initial OG concentration were 0.50 g L^{-1}, natural pH (5.6), and 10 mg L^{-1}, respectively. LFO shows negligible activity. During the dark adsorption step, approximately 5% of OG was adsorbed onto the LFO surface. Upon irradiation, a slight increase in the measured OG concentration was observed, likely due to partial desorption of weakly adsorbed dye molecules. As a result, the apparent concentration slightly exceeded 100% when normalized to the post-adsorption value. Thus, the initial C_0 concentration used at the onset of irradiation corresponds essentially to the non-adsorbed OG fraction. In comparison, the adsorption tests showed that bare g-CN, LFO/g-CN (1/0.5), LFO/g-CN (1/1), and LFO/g-CN (1/1.5) removed 1.9%, 6.1%, 7.4%, and 9.7% of OG dye, respectively. Under visible light irradiation, all the heterojunction photocatalysts outperformed bare g-CN. In Fig. 6a photocatalytic efficiency increased steadily with higher g-CN loading. After 135 min of irradiation, bare g-CN, LFO/g-CN (1/0.5), LFO/g-CN

© 2026 The Author(s). Published by the Royal Society of Chemistry

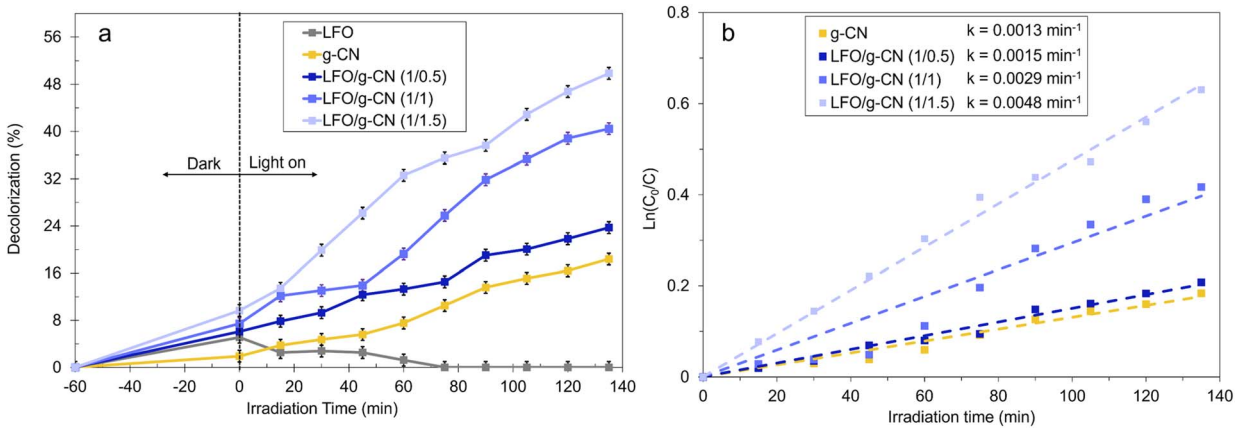


Fig. 6 (a) Adsorption and photocatalytic activities of LFO, g-CN, and LFO/g-CN (*x*/*y*) heterojunctions (with *x*/*y*: 1/0.5; 1/1 : 1/1.5) for OG degradation under visible light irradiation; (b) plot of Ln(C_0/C) *vs.* the irradiation time. (OG concentration = 10 mg L^{-1}, catalyst concentration = 0.50 g L^{-1}, T = 25 °C, pH 5.6, and visible-light intensity = 0.95 W cm^{-2}).

(1/1), and LFO/g-CN (1/1.5) achieved a removal percentage of 18.4%, 23.7%, 40.5% and 49.9%, respectively. The improved photocatalytic activity of the LFO/g-CN heterojunctions can be attributed to the combined effect of textural, optical, and interfacial properties. The LFO/g-CN (1/1.5) composite exhibits the highest BET specific surface area, 51 m^2 g^{-1}, which can provide more accessible active sites. In addition, FE-SEM/EDS observations confirm the formation of LFO/g-CN heterojunction regions, while UV-Vis analysis shows extended visible-light absorption. Based on the literature, these features could favour charge transfer and limit electron–hole recombination, thereby enhancing OG photocatalytic degradation.[48] Therefore, LFO/g-CN (1/1.5) was selected for further evaluation under different experimental conditions.

It is well known that the photocatalytic degradation of dyes is essentially described by a pseudo-first-order kinetic model.[49,50] The rate constant k can be determined by the following equation (eqn (1)):

$$\ln\left(\frac{C_0}{C}\right) = k \cdot t \quad (1)$$

where; C is the residual concentration of OG; C_0 is the initial concentration of OG, and t is the irradiation time.

Table 2 Rate constant values of the LFO/g-CN (*x*/*y*) heterojunctions, compared to those of pure g-CN for OG degradation under visible light irradiation

Photocatalyst	k (min^{-1})	R^2 [a]	% OG decolorization
Pure g-CN	$(13 \pm 0.4) \times 10^{-4}$	0.9704	18.4
LFO/g-CN (1/0.5)	$(15 \pm 0.4) \times 10^{-4}$	0.9834	23.7
LFO/g-CN (1/1)	$(29 \pm 2.0) \times 10^{-4}$	0.9358	40.5
LFO/g-CN (1/1.5)	$(48 \pm 0.7) \times 10^{-4}$	0.9927	49.9

[a] The values of R^2 > 0.97 reflect a fair agreement between the experimental data and the adopted first-order kinetic model.

The rate constants, k, were determined from the slope of the ln(C_0/C) *vs.* t curves (Fig. 6b), and were found to be 0.0013, 0.0015, 0.0029, and 0.0048 min^{-1} for g-CN, LFO/g-CN (1/0.5), LFO/g-CN (1/1), and LFO/g-CN(1/1.5), respectively (Table 2). Such values further confirm that the LFO/g-CN (1/1.5) composite exhibits the highest rate constant, nearly 3.8 times greater than that of pristine g-CN.

Recent investigations have consistently shown that perovskite/g-C_3N_4 heterojunctions enhance visible-light photocatalysis. For example, Humayun *et al.*[51] achieved 87–94% degradation of methylene blue (MB) and Rhodamine B (RhB) within 120 min using an LFO/g-CN Z-scheme, while Xu *et al.*[52] confirmed the synergistic effect of $LaFeO_3$/g-C_3N_4 coupling. Other ternary architectures such as α-Fe_2O_3/g-C_3N_4/Fe_3O_4 (ref. 34) and Ag_3PO_4/g-C_3N_4/CQDs[53] have also shown higher apparent rate constants (0.022 and 0.0247 min^{-1}, respectively), though differences in dye selection, catalyst design, and experimental conditions account for these values. More recently, Vasvini *et al.*[54] demonstrated efficient OG degradation using transition- and rare-earth-metal oxide-supported g-C_3N_4, emphasizing that interfacial engineering and optimized semiconductor ratios are crucial. Across recent literature, pristine g-C_3N_4 usually displays apparent rate constant (k_{app}) values in the order of 10^{-3} min^{-1} under visible/solar conditions, *e.g.*, 0.0044 min^{-1} for tetracycline (TC)[33] and 0.0057 min^{-1} for MB,[16] which is consistent with the reported 0.0013 min^{-1} baseline in this study and indicates that unmodified g-C_3N_4 provides a conservative benchmark for performance comparison (Table 3). The LFO/g-CN (1/1.5) heterojunction developed here achieves a comparable value of 0.0048 min^{-1}, indicating that this perovskite/g-C_3N_4 interface performs on par with other effective g-CN-based systems under visible-light irradiation.

The LFO/g-CN composite with the optimal mass ratio of 1 : 1.5, which provided the best photocatalytic performance, was further investigated to examine the effects of the four main operational parameters on the photocatalytic degradation of

© 2026 The Author(s). Published by the Royal Society of Chemistry

Table 3 Photocatalytic performance of g-C_3N_4 and related heterostructures under visible light. (RhB: Rhodamine B; MB: Methylene Blue)

Photocatalyst	Dye	k (min^{-1})	Decolorization time (min)	Ref.
Pure g-C_3N_4	OG	0.0013	135	This work
LFO/g-C_3N_4 (1/1.5)	OG	0.0048	135	This work
LFO/g-C_3N_4	MB, RhB	~0.008–0.010	120	51
LFO/g-C_3N_4	RhB	NR	150	52
α-Fe_2O_3/g-C_3N_4/Fe_3O_4	MB	0.091	60	34
Ag_3PO_4/g-C_3N_4/CQDs	RhB	0.0247	120	53
Transition/rare-earth oxide@g-C_3N_4	OG	NR	150	54
Pure g-C_3N_4	MB	0.0057	300	16

OG: catalyst concentration, solution pH, initial pollutant concentration, and visible-light irradiation intensity.

Effect of catalyst concentration

To investigate the effect of LFO/g-CN (1/1.5) catalyst concentration on the OG photocatalytic degradation, experiments were conducted with different catalyst loadings ranging from 0.25 to 1.50 g L^{-1} in a 10 mg L^{-1} OG solution. The effect of catalyst concentration on the OG photocatalytic decolorization kinetics, shown in Fig. 7a, reveals that photocatalytic efficiency improves as the catalyst concentration increases from 0.25 to 0.50 g, whereas beyond this optimal value, it declines. As summarized in Table 4, the highest removal percentage (50%) is achieved at a concentration of 0.5 g L^{-1}. The corresponding kinetic study (Fig. 8a) follows the same trend: k increases from 0.0009 min^{-1} at 0.25 g L^{-1} to 0.0048 min^{-1} at 0.50 g L^{-1}, then declines sharply at higher loadings (0.0013 min^{-1} at 1.50 g L^{-1}), indicating a reduction in photocatalytic activity.

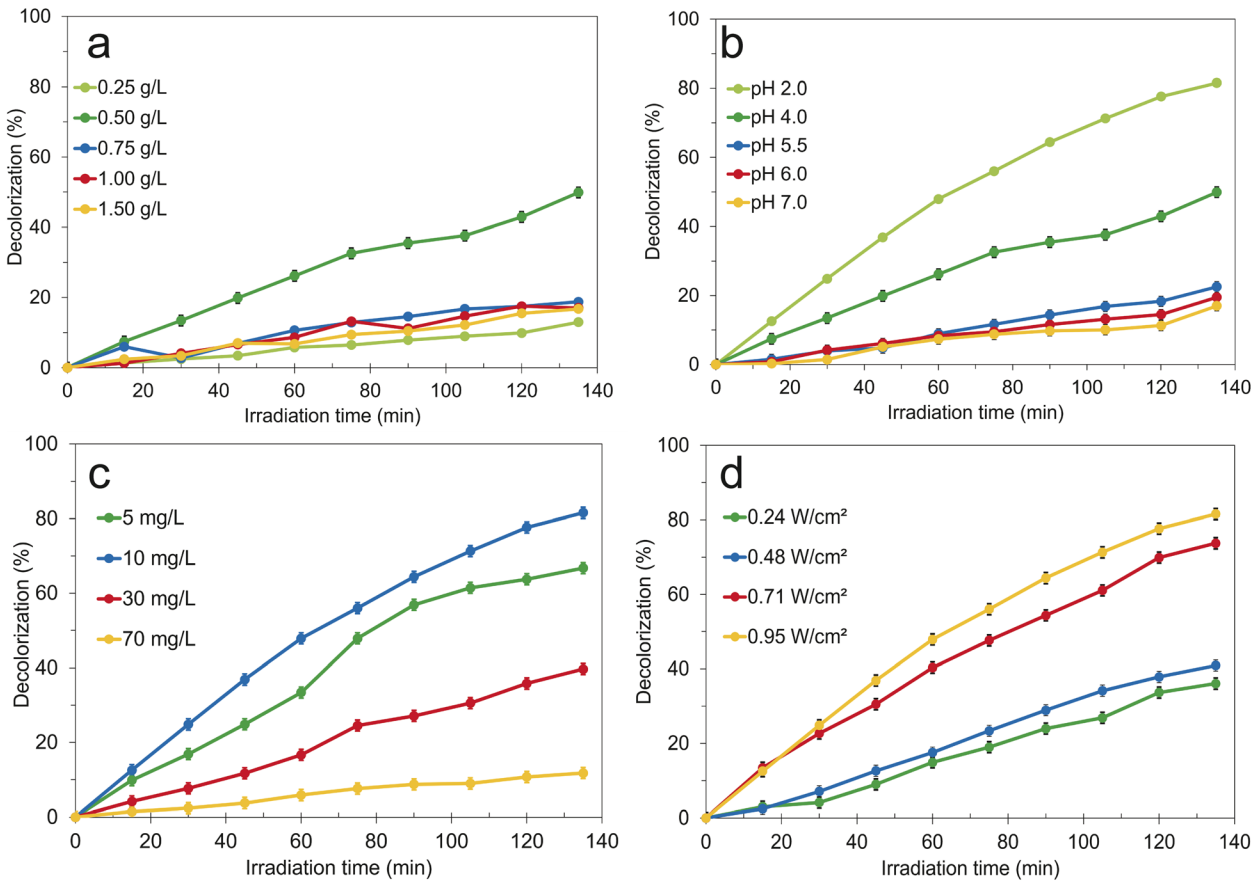


Fig. 7 Effect of main operational parameters on OG photocatalytic degradation using the LFO/g-CN (1/1.5) composite. (a) Effect of catalyst concentration (OG concentration = 10 mg L^{-1}, natural pH, T = 25 °C, and visible-light intensity = 0.95 W cm^{-2}); (b) effect of initial pH (OG concentration = 10 mg L^{-1}, catalyst concentration = 0.50 g L^{-1}, T = 25 °C, and Visible-light intensity = 0.95 W cm^{-2}); (c) effect of pollutant initial concentration (pH = 2.0, catalyst concentration = 0.50 g L^{-1}, T = 25 °C, and visible-light intensity = 0.95 W cm^{-2}), (d) effect of visible light intensity (OG concentration = 10 mg L^{-1}, pH = 2.0, catalyst concentration = 0.50 g L^{-1}, T = 25 °C).

© 2026 The Author(s). Published by the Royal Society of Chemistry

Table 4 Values of rate constants (k), correlation coefficient (R^2), and OG degradation efficiency regarding the four parameters studied (the effect of catalyst concentration, the effect of solution pH, the effect of initial pollutant concentration, and the effect of visible light intensity) for the LFO/g-CN (1/1.5) photocatalyst

Studied parameter	k (min^{-1})	R^2	OG decolorization efficiency (%)
Catalyst concentration (g L^{-1})			
0.25	$(9 \pm 0.2) \times 10^{-4}$	0.9807	13
0.50	$\mathbf{(48 \pm 0.7) \times 10^{-4}}$	**0.9927**	**50**
0.75	$(17 \pm 0.7) \times 10^{-4}$	0.9501	19
1.00	$(15 \pm 0.5) \times 10^{-4}$	0.9624	17
1.50	$(13 \pm 0.3) \times 10^{-4}$	0.9825	17
Solution pH			
2.0	$\mathbf{(119 \pm 2) \times 10^{-4}}$	**0.9883**	**82**
4.0	$(48 \pm 0.7) \times 10^{-4}$	0.9927	47
5.5	$(17 \pm 0.7) \times 10^{-4}$	0.9741	23
6.0	$(14 \pm 0.5) \times 10^{-4}$	0.9727	20
7.0	$(12 \pm 0.6) \times 10^{-4}$	0.9481	17
Initial polluant concentration (mg L^{-1})			
5	$(84 \pm 2) \times 10^{-4}$	0.9755	68
10	$\mathbf{(119 \pm 2) \times 10^{-4}}$	**0.9883**	**82**
30	$(36 \pm 0.8) \times 10^{-4}$	0.9843	40
70	$(10 \pm 0.2) \times 10^{-4}$	0.9883	12
Visible light intensity (W cm^{-2})			
0.24 (1 lamp)	$(31 \pm 1) \times 10^{-4}$	0.9629	36
0.48 (2 lamps)	$(38 \pm 1) \times 10^{-4}$	0.9801	42
0.71 (3 lamps)	$(94 \pm 2) \times 10^{-4}$	0.9860	74
0.95 (4 lampS)	$\mathbf{(119 \pm 2) \times 10^{-4}}$	**0.9883**	82

This behaviour can be rationalized by considering two competing effects. On the one hand, increasing the catalyst loading increases the number of active sites and the generation of electron–hole pairs, thereby improving the degradation rate. On the other hand, excessive catalyst concentrations lead to particle agglomeration and increased scattering, limiting light penetration into the suspension and ultimately suppressing photocatalytic performance. Moreover, at excessive catalyst loadings, the formation of particle aggregates may also reduce the distance between photogenerated electrons and holes, thereby promoting their recombination and further contributing to the decrease in the apparent rate constant. This behaviour is consistent with the well-known "screening effect" in heterogeneous photocatalysis.[55]

Effect of pH

The solution pH is a critical parameter for photocatalytic performance because it influences not only the catalyst's surface charge,[37] but also the nature of interactions with the dye molecules.[56–58] In this context, the effect of initial pH on the OG photocatalytic degradation kinetics was investigated using the LFO/g-CN (1/1.5) composite at a catalyst loading of 0.5 g L^{-1} (the optimized concentration) in an OG solution with an initial concentration of 10 mg L^{-1} (Fig. 7b). The pH of the OG solution was adjusted from 2.0 to 7.0 using 0.1 M HCl and 0.1 M NaOH before photocatalytic experiments. Fig. 8b shows the kinetic behaviour as a function of the solution's initial pH. The results, presented in Table 4, reveal a strong dependence of the photocatalytic efficiency and the kinetic rate constants on the solution's initial pH. At pH 2.0, the composite achieved the highest OG decolorization (82%) with a corresponding rate constant of $k = 0.0119$ min^{-1}. As the pH increased to 4.0, both the photocatalytic efficiency and k decreased significantly (47%, $k = 0.0048$ min^{-1}). Under nearly-neutral conditions (pH 5.5–7.0), the photocatalytic performance dropped dramatically, with degradation efficiencies of 23%, 20%, and 17% and k values as low as 0.0012–0.0017 min^{-1}. These findings clearly identify pH = 2.0 as the optimal condition for OG removal under the tested parameters. This trend is consistent with recent reports investigating the effect of solution pH on OG adsorption using the LFO/g-CN (1/1.5) system, which showed improved OG adsorption at pH 2.0.[37] It is well established in the literature that adsorption plays a crucial role in the photocatalytic dye degradation: the greater the adsorption of dye molecules on the catalyst surface, the more effective the subsequent photocatalytic oxidation.

The influence of the initial solution pH on the photocatalytic degradation of OG dye can be attributed to the surface charge properties of the LFO/g-CN (1/1.5) composite and the acid–base speciation of the OG dye. The pH at the Point of Zero Charge (pH_{PZC}) of the catalyst, determined in a recent adsorption study, was 6.8.[37] This value indicates that at pH values below 6.8, the composite surface becomes positively charged, whereas at pH values above 6.8, it acquires a net negative charge. OG is an anionic dye containing sulfonate groups ($-SO_3^-$), which confer a negative charge in aqueous solution across the investigated pH range. Therefore, at acidic pH ($pH < pH_{PZC} = 6.8$),[37] the electrostatic attraction between the positively charged catalyst surface and the negatively charged OG molecules is enhanced, promoting greater adsorption of OG (*ca.* 38%) onto the catalyst surface. This increased adsorption facilitates the transfer of photogenerated reactive species ($OH^{\bullet}$, $O_2^{-\bullet}$, h^+) to the adsorbed dye molecules, accelerating their oxidative degradation. Conversely, at nearly neutral or alkaline pH ($pH \geq pH_{PZC}$), the catalyst surface becomes negatively charged, leading to electrostatic repulsion with the anionic OG species (inset Fig. 1), reducing adsorption and, consequently, lowering photocatalytic efficiency. This interplay between surface charge, dye ionization state, and adsorption behaviour explains the observed maximum degradation rate and efficiency at pH 2.0, followed by a marked decrease in performance as the solution pH approaches and exceeds the pH_{PZC}.

Comparing these findings with the recent literature confirms the competitive performance of the developed LFO/g-CN heterojunction under acidic conditions. For example, Mahir *et al.*[59] observed optimal OG dye adsorption (~95%) at slightly acidic pH over L-Arg-PPy@g-C_3N_4 (L-arginine-polypyrrole@g-C_3N_4), attributing the improvement to enhanced electrostatic adsorption. Similarly, Yaqoubi *et al.*[60] reported that the degradation of Eriochrome black T (EB) using $NiMn_2O_4$/g-C_3N_4 was highest at pH 4.0 and decreased sharply under basic conditions due to reduced dye-catalyst affinity.

© 2026 The Author(s). Published by the Royal Society of Chemistry

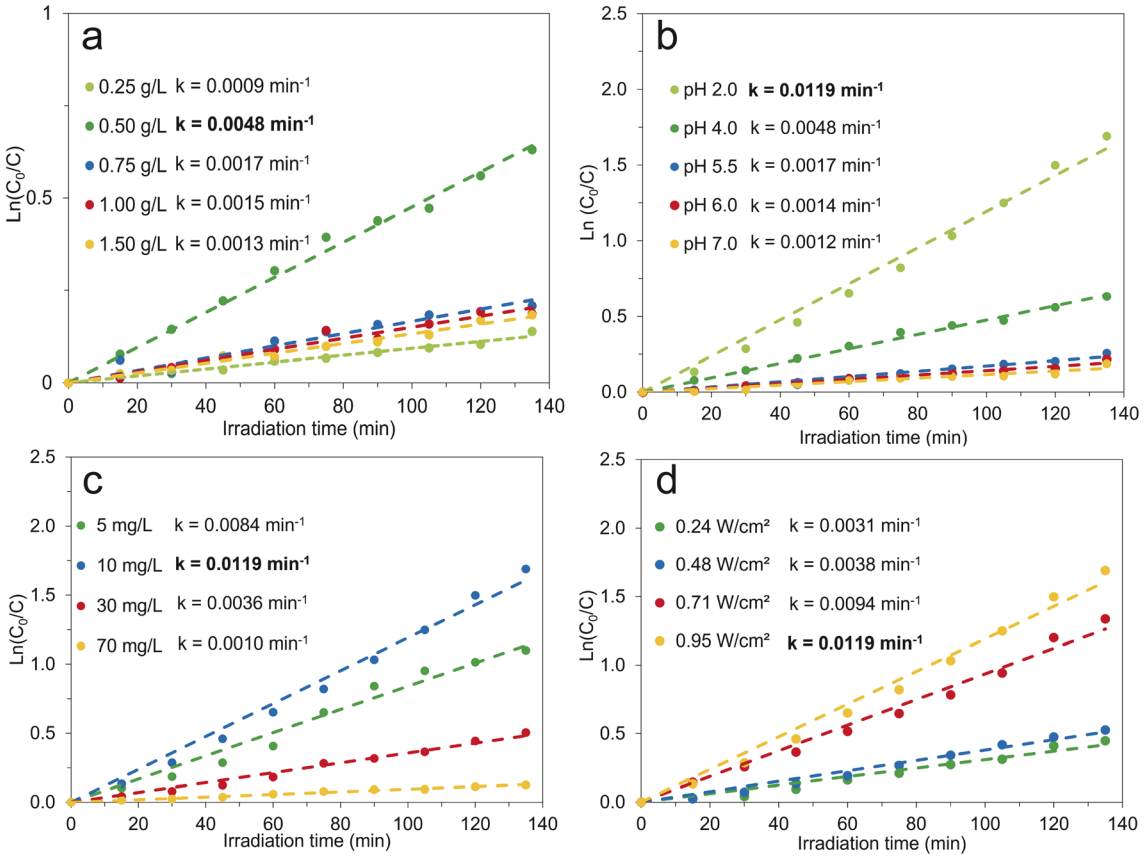


Fig. 8 Kinetic study as the effect of the main operational parameters on OG photocatalytic degradation using the LFO/g-CN (1/1.5) composite: (a) effect of catalyst concentration, (b) effect of solution pH, (c) effect of initial pollutant concentration, and (d) effect of visible light intensity.

Consistent with our observations, recent studies have shown that the influence of solution pH on photocatalytic degradation is mainly controlled by surface charge properties, charge-carrier behaviour, and the nature of the reactive species involved in the oxidation process. Chen *et al.*[61] reported that acidic conditions significantly enhanced RhB degradation over a Bi-based photocatalyst, achieving ~97% removal at pH 3.0, with total organic carbon (TOC) analysis confirming substantial mineralization (>58%). Their results showed that acidic media promoted the simultaneous involvement of $OH^{\bullet}$, $O_2^{-\bullet}$, h^+, whereas $OH^{\bullet}$ radicals dominated under near-neutral conditions. These findings suggest that reactive species generation, rather than simple dye accumulation, are responsible for enhanced photocatalytic activity at low pH, consistent with the higher OG degradation observed for the LFO/g-CN composite in the present study. Although pH 2.0 yields the highest OG decolorization efficiency in this study, the sharp decrease observed near neutral pH indicates that further optimization would be required for real wastewater applications without extensive pH adjustment.

Effect of pollutant initial concentration

Experimental data on the effect of the initial pollutant concentration on the OG photocatalytic degradation kinetics over the LFO/g-CN (1/1.5) heterojunction are illustrated in Fig. 7c, 8c and Table 4. Four dye concentrations were chosen: 5 mg L^{-1}, 10 mg L^{-1}, 30 mg L^{-1}, and 70 mg L^{-1}.

The photocatalytic efficiency initially increased with pollutant concentration before decreasing sharply at higher concentrations. At 5 mg L^{-1}, the degradation efficiency reached 68% with a rate constant $k = 0.0084$ min^{-1}. At 10 mg L^{-1}, k increases to 0.0119 min^{-1}, corresponding to 82% OG decolorization (maximum observed). However, at higher pollutant concentrations, the photocatalytic activity decreased significantly: at 30 mg L^{-1}, the efficiency dropped to 40% with $k = 0.0036$ min^{-1}, while at 70 mg L^{-1}, only 12% removal was achieved with $k = 0.0010$ min^{-1}.

This trend indicates that low-to-moderate pollutant concentrations promote efficient dye–catalyst interactions, whereas higher concentrations block light penetration, saturate active sites, and scavenge reactive species. These findings are consistent with general photocatalytic mechanisms reported in the literature, in which increasing pollutant concentration shortens the photon path length in solution. At high pollutant concentrations, a significant amount of light may be absorbed by the pollutant molecules rather than by the catalyst, thereby reducing catalytic efficiency.[62–64] Importantly, the maximum k value obtained in this study (0.0119 min^{-1} at 10 mg L^{-1}) is of the same order as those reported for other g-

© 2026 The Author(s). Published by the Royal Society of Chemistry

C_3N_4-based heterojunctions, confirming the effectiveness of the LFO/g-CN (1/1.5) system while emphasizing the need to optimize pollutant concentration for practical applications.

Effect of visible light intensity

To evaluate the effect of visible light intensity on the OG photocatalytic degradation using the LFO/g-CN (1/1.5) composite, experiments were conducted at pH 2.0 under different visible light intensities. Four intensities were chosen: 0.24 W cm^{-2} (one lamp), 0.48 W cm^{-2} (two lamps), 0.71 W cm^{-2} (three lamps), and 0.95 W cm^{-2} (four lamps).

Fig. 7d and 8d illustrate the experimental data for the OG photocatalytic decolorization and its kinetic study at varying visible-light intensities, respectively. The results (Table 4) demonstrate that degradation efficiency and kinetic rate constants increase markedly with higher light intensity. At the lowest intensity (0.24 W cm^{-2}), the degradation efficiency reached 36% with a very small rate constant ($k = 0.0031$ min^{-1}). Increasing the intensity to 0.48 W cm^{-2} slightly improved both the degradation efficiency to 42% and the rate constant to 0.0038 min^{-1}. A more pronounced enhancement was observed at 0.71 W cm^{-2}, where the degradation efficiency increased to 74%, and k rose to 0.0094 min^{-1}. The best performance was observed at 0.95 W cm^{-2} (four lamps), yielding a decolorization efficiency of 82% and a maximum rate constant of 0.0119 min^{-1}. This enhancement is attributed to the higher photon flux, which probably generates more electron–hole pairs and reactive oxygen species, thus accelerating dye breakdown. Similar intensity-dependent improvements in photocatalytic activity have been observed in other systems.[65,66] Previous studies have shown that increasing irradiation improves degradation rates due to enhanced charge carriers generation,[67] although performance may decline beyond an optimal intensity because of thermal effects.[68] These results demonstrate that the LFO/g-CN (1/1.5) composite effectively harnesses strong light intensities without significant recombination losses, validating its suitability for visible-light photocatalysis.

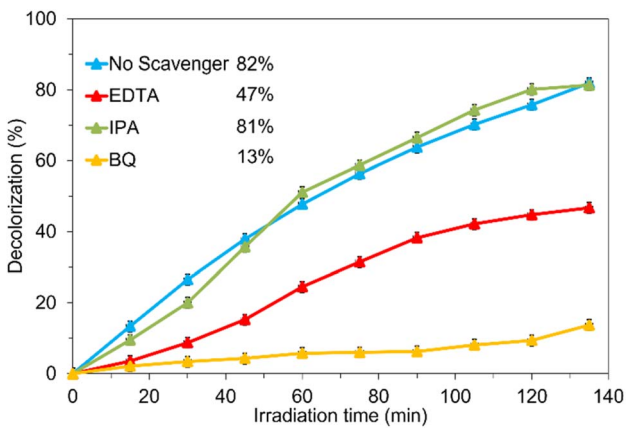


Fig. 9 Effect of scavengers of OH˙ radicals, holes, and $O_2^{-\bullet}$ radicals on OG photocatalytic degradation using LFO/g-CN (1/1.5) composite under visible light irradiation.

Reaction mechanism

As shown in Fig. 9, several scavenger experiments were conducted to identify the primary reactive species involved in the photocatalytic degradation of OG over LFO/g-CN (1/1.5). In the absence of scavengers, the degradation efficiency reached 82%. The addition of EDTA and BQ scavengers significantly reduced the OG degradation efficiency to 47% and 13%, respectively. This suggests that holes (h^+) and, more importantly, $O_2^{-\bullet}$ radicals contribute significantly to the total OG degradation. By contrast, the addition of IPA caused only a negligible decrease in OG degradation (from 82 to 81%), suggesting that OH˙ radicals do not significantly contribute under the present conditions.[69] Therefore, the photocatalytic degradation of OG is mainly driven by $O_2^{-\bullet}$ radicals, with a secondary contribution from h^+.

HPLC-MS analysis of OG degradation intermediates

To further support the chemical transformation of OG during photocatalysis, HPLC-MS analyses were performed on solutions collected at different irradiation times under the optimized conditions. The sample labelled as $t = 0$ min corresponds to the suspension after 1 h of dark equilibration with the LFO/g-CN photocatalyst, immediately before switching on the light. During this step, the OG concentration decreased of about 10%, indicating partial adsorption of OG on the photocatalyst surface under acidic conditions. Upon visible-light irradiation, the parent OG signal, detected as the free-acid form at m/z 407 in ESI(–) and m/z 409 in ESI(+) (Fig. S2a and b) progressively decreased over time. In ESI(+) mode, fragments at m/z 391 and 327 were tentatively assigned to dehydration and sulfonate-loss/desulfonation-related fragmentation of the parent OG molecule, respectively (Fig. S2c and Table S1). Several lower-m/z signals appeared or changed in intensity.[70] At low-retention-time a signal was already observed at $t = 0$ min, likely due to an early transformation product formed during dark contact. In ESI(–) mode, additional lower m/z ions, including those at m/z 257 and 243, showed fragmentation compatible with sulfonated aromatic intermediates (Fig. S2d and e).[70,71] Moreover, minor signals with chlorine-compatible isotopic patterns were also detected and may be related to chloride ions introduced by HCl during pH adjustment. After 135 min of irradiation, no signal attributable to the parent OG molecule was detected (Fig. 10). Consistently, the HPLC-UV-vis chromatogram did not show the OG peak at this irradiation time. Only a peak at very low retention time, around 1 min, remained, which could be tentatively ascribed to small polar degradation products, such as short-chain carboxylic acids.

Stability and reusability of the LFO/g-CN (1/1.5) photocatalyst

The stability and reusability of the LFO/g-CN (1/1.5) photocatalyst were tested over four successive cycles for OG degradation. As shown in Fig. 11, efficiency decreased only slightly, from 82% in the first cycle to 77% after the fourth run, corresponding to a 6% drop. This result indicates that the photocatalyst retains most of its activity after repeated use. Post-

© 2026 The Author(s). Published by the Royal Society of Chemistry

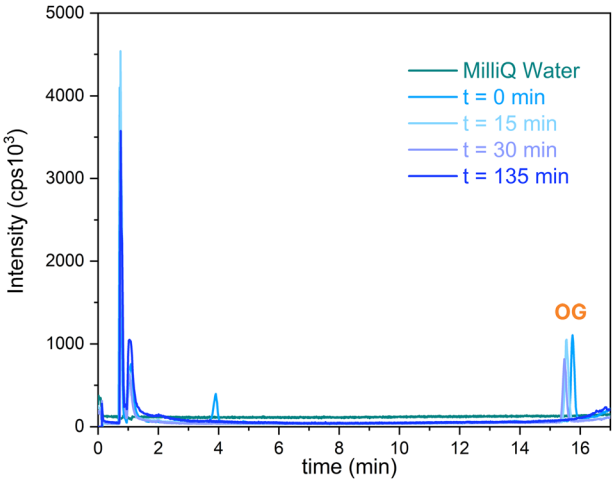


Fig. 10 HPLC-MS chromatograms in ESI(−) mode of OG solutions collected during the photocatalytic degradation of OG over LFO/g-CN (1/1.5) under optimized conditions. The $t = 0$ min sample was collected after 1 h of dark equilibration, immediately before irradiation.

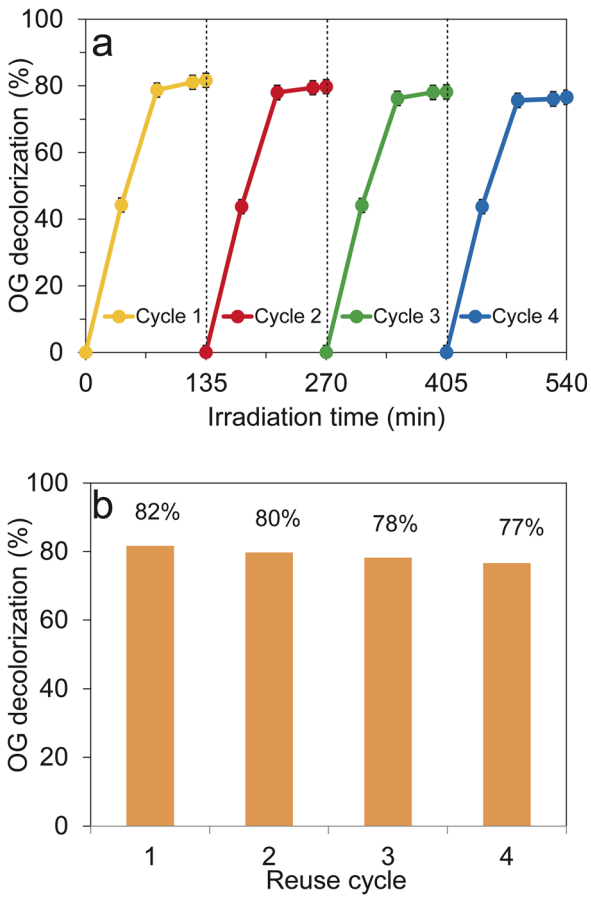


Fig. 11 (a) Photocatalytic experiments using recycled LFO/g-CN (1/1.5) for OG degradation and (b) OG photocatalytic decolorization percentages for four consecutive cycles over regenerated LFO/g-CN (1/1.5).

reaction characterization revealed that the material was not completely unchanged after the photocatalytic cycles. XRD/Rietveld analysis showed an approximately 38 wt% decrease in the relative amount of the LFO phase, while ICP-MS analysis of the recovered powder indicated a decrease in La content of around 30% compared with the fresh material (Fig. S3a). A decrease in the La surface content was also evidenced by XPS analysis (not reported). This suggests partial La depletion under the acidic reaction conditions.[72] Such behaviour is consistent with the $LaFeO_3$ structure, where La^{3+} occupies the A-site of the perovskite lattice, whereas Fe^{3+} is located in the B-site FeO_6 octahedral framework; the A-site cation is generally more susceptible to acid-driven depletion than the B-site cation embedded in the octahedral network.[72] Nevertheless, FE-SEM/EDS elemental maps of the recovered sample still showed regions where both LFO and g-CN coexist, suggesting that interfacial contact between the two phases was at least partially preserved after reuse (Fig. S3b). Moreover, the valence-band XPS profiles of the fresh and recovered LFO/g-CN (1/1.5) samples were very similar, with the VB onset remaining approximately unchanged at around 0.7 eV before and after the photocatalytic cycles (Fig. S3c) This indicates that, despite partial La depletion, the surface electronic structure of the heterojunction was largely preserved after reuse and these remaining LFO/g-CN contact regions were likely sufficient to maintain an overall good photocatalytic activity. Comparable studies have also reported the high reusability of perovskite/g-CN heterostructures, with only minor reductions in activity after multiple cycles,[47] confirming that they are suitable for long-term wastewater treatment applications.[33,73]

Conclusions

In this work, graphitic carbon nitride (g-CN), lanthanum ferrite (LFO), and their heterojunction composites (LFO/g-CN) were successfully synthesized using scalable, straightforward methods: thermal polymerization, sol–gel, and wet impregnation.

Physico-chemical characterization of the samples showed a mutually beneficial effect of the two pristine materials. On the one hand, the presence of g-CN flakes increases the composites' surface area and porosity, ultimately favouring diffusion phenomena relevant to photocatalytic applications. On the other hand, LFO extends light absorption in the visible range. Additional PL and XPS analyses further supported the occurrence of an interaction between the two semiconductors, in that the presence of g-CN deeply affected the electronic properties of the final composite.

Accordingly, preliminary photocatalytic experiments demonstrated that coupling LFO with g-CN significantly enhances the OG dye removal under visible-light irradiation compared with pristine g-CN and perovskite-type LFO. The LFO/g-CN (1/1.5) composite exhibited the highest degradation efficiency (50%) and rate constant (0.0048 min^{-1}), approximately 3.8 times higher than that of pristine g-CN (0.0013 min^{-1}). This superior performance was mainly attributed to extended light

© 2026 The Author(s). Published by the Royal Society of Chemistry

harvesting and synergistic interfacial interactions within the heterostructure.

Afterward, several operational parameters affecting the photocatalytic degradation of OG were evaluated. The results reveal that an optimal catalyst loading (0.5 g L^{-1}), an acidic medium (pH 2.0), an initial pollutant concentration (10 mg L^{-1}), and a visible light intensity (0.95 W cm^{-2}) collectively promote an efficient photocatalytic decolorization of 82% with a high rate constant of 0.0119 min^{-1}. HPLC-UV-Vis and HPLC-MS analyses confirmed that the parent OG molecule was no longer detected after 135 min under these optimized conditions, although the formation of lower-molecular-weight transformation products indicates that a complete mineralization was not reached. At higher catalyst loading or pollutant concentration, or under near-neutral conditions, the photocatalytic activity declined due to light scattering, surface saturation, and electrostatic repulsion, respectively.

Experiments carried out with three types of radical scavengers showed that superoxide radicals ($O_2^{-\bullet}$) are the dominant reactive species responsible for OG degradation, followed by photogenerated holes (h^+) while hydroxyl radical ($OH^\bullet$) play only a minor role. These results provide further insight into the reaction pathway and support the involvement of both oxidative radical and hole-driven processes.

The LFO/g-CN (1/1.5) composite also showed excellent reusability, retaining ~94% of its activity after four consecutive cycles, notwithstanding some physico-chemical and compositional changes, as detected by post-reaction analysis. While post-reaction XRD/Rietveld and ICP-MS analyses revealed partial changes in the LFO component, likely promoted by the very acidic reaction conditions, FE-SEM/EDS maps showed that regions containing both LFO and g-CN were still present after reuse. In addition, VB-XPS analysis showed that the valence-band onset of the recovered heterojunction remained approximately unchanged. These results suggest that sufficient interfacial contact was preserved to maintain good photocatalytic activity. Overall, our findings highlight the potential of perovskite-g-CN coupling as a promising strategy for designing cost-effective, solar-active photocatalysts for sustainable wastewater treatment and environmental remediation.

Author contributions

Hinane Baleh: investigation, formal analysis, writing – original draft; Naziha Chakour: investigation, formal analysis, writing – original draft; Khaled Djakhdane: investigation, formal analysis, writing – original draft Salah Bassaid: methodology, visualization, conceptualization; writing – review and editing; resources, supervision Abdelkader Dehbi: methodology, visualization, conceptualization; writing – review and editing; resources, project administration, supervision. Nadir Ouldhamadouche investigation, formal analysis, writing – original draft; Francesca S. Freyria: investigation, visualization; conceptualization, writing – original draft, writing – review and editing; supervision; Barbara Bonelli: methodology, visualization, conceptualization; writing – original draft, writing – review and editing, resources, supervision. Marco Coha- investigation, formal analysis, writing – original draft; Nicoletta Ditaranto investigation, formal analysis, writing – original draft Ali Alsalme: investigation, formal analysis, writing – original draft.

Conflicts of interest

There are no conflicts to declare.

Data availability

The data presented in this work are available in the article and in the supplementary information (SI) file. Additional information/data related to this study are available upon request from the corresponding authors. Supplementary information: additional UV-vis spectra recorded during the photocatalytic experiments under different operating conditions, HPLC-MS chromatograms and related data on the photocatalytic transformation of the OG molecule and complementary characterization data for the LFO/g-CN photocatalyst afterrecycling cycles. See DOI: https://doi.org/10.1039/d6ra02138g.

Acknowledgements

Dr Salvatore Guastella and Dr Carla Celozzi from the Department of Applied Science and Technology of Politecnico di Torino (Italy) are acknowledged for the FE-SEM measurements and EDS maps and ICP-MS analysis, respectively. This study received financial support from the Faculty of Material Sciences, Ibn Khaldoun University of Tiaret. The authors would like to acknowledge the Ongoing Research Funding Program, (ORF-2026-78), King Saud University, Riyadh, Saudi Arabia.

References

1 D. Ma, H. Yi, C. Lai, X. Liu, X. Huo, Z. An, L. Li, Y. Fu, B. Li, M. Zhang, L. Qin, S. Liu and L. Yang, *Chemosphere*, 2021, **275**, 130104, DOI: 10.1016/j.chemosphere.2021.130104.

2 F. S. Freyria, F. Sannino and B. Bonelli, *Nanomater. Detect. Removal Wastewater Pollut.*, 2020, **50**, 19–46, DOI: 10.1016/B978-0-12-818489-9.00002-5.

3 M. Compagnoni, G. Ramis, F. S. Freyria, M. Armandi, B. Bonelli and I. Rossetti, *J. Nanosci. Nanotechnol.*, 2017, **17**, 3632–3653, DOI: 10.1166/jnn.2017.14006.

4 F. S. Freyria, M. Armandi, M. Compagnoni, G. Ramis, I. Rossetti and B. Bonelli, *J. Nanosci. Nanotechnol.*, 2017, **17**, 3654–3672, DOI: 10.1166/jnn.2017.14014.

5 A. Bouazza, S. Bassaid, A. Dehbi, A. Guarnaccio and M. D'Auria, *React. Kinet., Mech. Catal.*, 2023, **136**, 1589–1605, DOI: 10.1007/s11144-023-02400-4.

6 H. Baleh, S. Bassaid, A. Dehbi, A. Benaouda, A. Bouazza, A. Alsalme, B. Bonelli and M. Messori, *React. Kinet., Mech. Catal.*, 2024, **137**, 2827–2845, DOI: 10.1007/s11144-024-02669-z.

7 N. Blangetti, F. S. Freyria, M. C. Calviello, N. Ditaranto, S. Guastella and B. Bonelli, *Catalysts*, 2023, **13**, 434, DOI: 10.3390/catal13020434.

© 2026 The Author(s). Published by the Royal Society of Chemistry

8 M. Pelaez, N. T. Nolan, S. C. Pillai, M. K. Seery, P. Falaras, A. G. Kontos, P. S. M. Dunlop, J. W. J. Hamilton, J. A. Byrne, K. O'Shea, M. H. Entezari and D. D. Dionysiou, *Appl. Catal., B*, 2012, **125**, 331–349, DOI: 10.1016/j.apcatb.2012.05.036.

9 M. N. Chong, B. Jin, C. W. K. Chow and C. Saint, *Water Res.*, 2010, **44**, 2997–3027, DOI: 10.1016/j.watres.2010.02.039.

10 N. Blangetti, F. S. Freyria, M. Manzoli, P. Rivolo, A. Piovano, H. Darjazi, N. Ditaranto, B. Patrizi, S. Doria and B. Bonelli, *Appl. Surf. Sci. Adv.*, 2025, **30**, 100896, DOI: 10.1016/j.apsadv.2025.100896.

11 J. Wen, J. Xie, X. Chen and X. Li, *Appl. Surf. Sci.*, 2017, **391**, 72–123, DOI: 10.1016/J.APSUSC.2016.07.030.

12 X. Guo, J. Duan, C. Li, Z. Zhang and W. Wang, *J. Mater. Sci.*, 2020, **55**, 2018–2031, DOI: 10.1007/s10853-019-04097-0.

13 Z. Chen, S. Zhang, Y. Liu, N. S. Alharbi, S. O. Rabah, S. Wang and X. Wang, *Sci. Total Environ.*, 2020, **731**, 139054, DOI: 10.1016/j.scitotenv.2020.139054.

14 J. Zhao, X. Cao, Y. Bai, J. Chen and C. Zhang, *Opt. Mater.*, 2023, **135**, 113239, DOI: 10.1016/j.optmat.2022.113239.

15 H. Guo, S. Wan, Y. Wang, W. Ma, Q. Zhong and J. Ding, *Chem. Eng. J.*, 2021, **412**, 128646, DOI: 10.1016/j.cej.2021.128646.

16 Y. Alaya, B. Chouchene, G. Medjahdi, L. Balan, N. Bouguila and R. Schneider, *Catalysts*, 2024, **14**, 226, DOI: 10.3390/catal14040226.

17 S. Pourali, R. Amrollahi, S. Alamolhoda and S. M. Masoudpanah, *Sci. Rep.*, 2024, **151**(15), 462, DOI: 10.1038/s41598-024-84645-0.

18 S. Qi, R. Zhang, Y. Zhang, X. Liu and H. Xu, *Inorg. Chem. Commun.*, 2021, **132**, 108761, DOI: 10.1016/j.inoche.2021.108761.

19 M. Humayun, H. Ullah, M. Usman, A. Habibi-Yangjeh, A. A. Tahir, C. Wang and W. Luo, *J. Energy Chem.*, 2022, **66**, 314–338, DOI: 10.1016/j.jechem.2021.08.023.

20 P. Hao, G. Qiu, P. Song, Z. Yang and Q. Wang, *Appl. Surf. Sci.*, 2020, **515**, 146025, DOI: 10.1016/j.apsusc.2020.146025.

21 Y. Zhang, J. Ding, W. Xu, M. Wang, R. Shao, Y. Sun and B. Lin, *Chem. Eng. J.*, 2020, **386**, 124030, DOI: 10.1016/j.cej.2020.124030.

22 A. Aizat, F. Aziz, M. N. Mohd Sokri, M. S. Sahimi, N. Yahya, J. Jaafar, W. N. Wan Salleh, N. Yusof and A. F. Ismail, *SN Appl. Sci.*, 2019, **1**, 91, DOI: 10.1007/s42452-018-0104-x.

23 S. Frangini, L. Della Seta and C. Paoletti, *Energies*, 2022, **15**, 632, DOI: 10.3390/en15020632.

24 Z. F. Gu, Y. J. Xu, B. Hong, J. C. Xu, Y. B. Han, H. X. Jin, D. F. Jin, X. L. Peng, J. Gong, H. L. Ge and X. Q. Wang, *Diamond Relat. Mater.*, 2023, **132**, 109685, DOI: 10.1016/J.DIAMOND.2023.109685.

25 C. Tan, C. Chen, W. Danni, X. Zhao, L. Zhou, X. Lu, J. Liang and W. Wang, *J. Alloys Compd.*, 2024, **1002**, 175211, DOI: 10.1016/j.jallcom.2024.175211.

26 Y. Wu, H. Wang, W. Tu, Y. Liu, Y. Z. Tan, X. Yuan and J. W. Chew, *J. Hazard. Mater.*, 2018, **347**, 412–422, DOI: 10.1016/j.jhazmat.2018.01.025.

27 C. Hu, B. Yu, Z. Zhu, J. Zheng, W. Wang and B. Liu, *Colloids Surf., A*, 2023, **664**, 131189, DOI: 10.1016/j.colsurfa.2023.131189.

28 I. Khan, M. Luo, L. Guo, S. Khan, S. A. Shah, I. Khan, A. Khan, C. Wang, B. Ai and S. Zaman, *Appl. Catal., A*, 2022, **629**, 118418, DOI: 10.1016/j.apcata.2021.118418.

29 K. Mazloomi and C. Gomes, *Int. J. Hydrogen Energy*, 2020, **45**, 17468–17479, DOI: 10.1016/j.rser.2012.02.028.

30 Z. Jin, R. Hu, H. Wang, J. Hu and T. Ren, *Appl. Surf. Sci.*, 2019, **491**, 432–442, DOI: 10.1016/j.apsusc.2019.06.143.

31 C. Ye, R. Wang, H. Wang and F. Jiang, *BMC Chem.*, 2020, **141**(14), 65, DOI: 10.1186/s13065-020-00719-w.

32 X. Tong, X. T. Kong, Y. Zhou, F. Navarro-Pardo, G. S. Selopal, S. Sun, A. O. Govorov, H. Zhao, Z. M. Wang and F. Rosei, *Adv. Energy Mater.*, 2018, **8**, 1–11, DOI: 10.1002/aenm.201701432.

33 S. Gao, Y. Liu, J. Zhu, Y. Wang, X. Han, X. Xia and X. Zhao, *Environ. Sci.: Water Res. Technol.*, 2021, **7**, 1430–1442, DOI: 10.1039/d1ew00026h.

34 M. Afkari, S. M. Masoudpanah, M. Hasheminiasari and S. Alamolhoda, *Sci. Rep.*, 2023, **131**(13), 6203, DOI: 10.1038/s41598-023-33338-1.

35 L. li Zheng, X. yan Xiao, Y. Li and W. Zhang, *Trans. Nonferrous Met. Soc. China*, 2017, 1117–1126, DOI: 10.1016/S1003-6326(17)60130-4.

36 B. Purusottam Reddy, E. Ravindran, P. Rosaiah, M. R. Karim, Y. Suh, S. H. Park and R. Mangiri, *Ceram. Int.*, 2025, **51**, 51723–51733, DOI: 10.1016/J.CERAMINT.2025.08.285.

37 N. Chakour, H. Baleh, S. Bassaid, A. Dehbi, N. Oueld hamadouche, G. Colucci, F. S. Freyria, B. Bonelli, A. Alsalme and M. Messori, *React. Kinet., Mech. Catal.*, 2025, **138**, 2575–2595, DOI: 10.1007/s11144-025-02870-8.

38 M. Ismael, Y. Wu, D. H. Taffa, P. Bottke and M. Wark, *New J. Chem.*, 2019, **43**, 6909–6920, DOI: 10.1039/C9NJ00859D.

39 Z. Li, W. Zhang, C. Yuan and Y. Su, *RSC Adv.*, 2017, **7**, 12931–12937, DOI: 10.1039/c6ra27423d.

40 K. Xu, H. Xu, G. Feng and J. Feng, *New J. Chem.*, 2017, **41**, 14602–14609, DOI: 10.1039/C7NJ03120C.

41 B. Li, T. Tian, Y. Zheng, D. Jiang, G. Xu, Y. Sun, Z. Li and Y. Yuan, *Chem.–Eur. J.*, 2025, **31**, e202500297, DOI: 10.1002/CHEM.202500297.

42 M. Lazemi, F. J. Mohammad, S. H. Park, A. Katoch, H. J. F. A. Blankesteijn, A. R. Botello-Méndez, E. van der Minne, Y. A. Birkhölzer, I. C. G. van den Bosch, E. M. Kiens, C. Baeumer, G. Koster, S. Kwon, U. Bergmann and F. M. F. de Groot, *Adv. Mater.*, 2025, **37**, 2502932, DOI: 10.1002/adma.202502932.

43 M. D. Scafetta, A. M. Cordi, J. M. Rondinelli and S. J. May, *J. Phys.: Condens. Matter*, 2014, **26**, 505502, DOI: 10.1088/0953-8984/26/50/505502.

44 L. You, F. Zheng, L. Fang, Y. Zhou, L. Z. Tan, Z. Zhang, G. Ma, D. Schmidt, A. Rusydi, L. Wang, L. Chang, A. M. Rappe and J. Wang, *Sci. Adv.*, 2018, **4**, 1–9, DOI: 10.1126/sciadv.aat3438.

45 R. Paudel, A. R. Burton, M. A. Kuroda, B. H. Farnum and R. B. Comes, *J. Vac. Sci. Technol., A*, 2023, **41**, 063207, DOI: 10.1116/6.0002987.

46 Y. Wang, W. Yang and K. Ding, *Molecules*, 2024, **29**, 3871, DOI: 10.3390/MOLECULES29163871.

© 2026 The Author(s). Published by the Royal Society of Chemistry

47 F. Safari, R. Poursalehi and H. Delavari, *RSC Adv.*, 2024, **14**, 26943–26953, DOI: 10.1039/D4RA00859F.
48 M. Yaqoubi, M. Ghanbari, E. A. Dawi, S. H. Ganduh, L. S. Jasim and M. Salavati-Niasari, *RSC Adv.*, 2026, **16**, 8709–8719, DOI: 10.1039/D5RA08965D.
49 S. Bassaid, D. Robert and M. Chaib, *Appl. Catal., B*, 2009, **86**, 93–97, DOI: 10.1016/J.APCATB.2008.07.027.
50 S. Bassaid, B. Ziane, M. Badaoui, M. Chaib and D. Robert, *Appl. Nanosci.*, 2012, **33**, 211–215, DOI: 10.1007/S13204-012-0108-6.
51 M. Humayun, A. Bahadur, A. Khan and M. Bououdina, *Catalysts*, 2023, **13**, 907, DOI: 10.3390/catal13050907.
52 K. Xu and J. Feng, *RSC Adv.*, 2017, **7**, 45369–45376, DOI: 10.1039/c7ra08715b.
53 Y. Wang, M. Ding, Z. Li and M. Li, *Surf. Interfaces*, 2024, **44**, 103585, DOI: 10.1016/j.surfin.2023.103585.
54 M. D. Vasvini, A. K. Rubesh, J. G. Joseph, B. Dhanalakshmi and J. G. Suganya, *Appl. Catal. O: Open*, 2024, **195**, 207009, DOI: 10.1016/j.apcato.2024.207009.
55 J. Mei, X. Gao, J. Zou and F. Pang, *Catalysts*, 2023, **13**(6), 974, DOI: 10.3390/catal13060974.
56 H. Zouggari, F. Z. Mahir, A. Imgharn, A. Hsini, N. Aarab, M. Laabd and A. Albourine, *Carbon Lett.*, 2023, **336**(33), 1897–1908, DOI: 10.1007/s42823-023-00513-3.
57 J. Zhang, C. Su, X. Xie, P. Liu and M. E. Huq, *RSC Adv.*, 2020, **10**, 37028–37034, DOI: 10.1039/d0ra05275b.
58 F. S. Freyria, S. Esposito, M. Armandi, F. Deorsola, E. Garrone and B. Bonelli, *J. Nanomater.*, 2017, **2017**, 1–13, DOI: 10.1155/2017/2749575.
59 F. Z. Mahir, H. Zouggari, A. Imgharn, A. A. Addi, K. A. El Bacha, A. M. Diez, M. Á. Sanromán, M. Laabd, A. Hsini, N. Aarab, L. Bazzi, R. Lakhmiri and A. Albourine, *Inorg. Chem. Commun.*, 2025, **172**, 113656, DOI: 10.1016/j.inoche.2024.113656.
60 M. Yaqoubi, M. Ghanbari, R. W. Maya, H. A. Jasim and M. Salavati-Niasari, *Results Eng.*, 2025, **25**, 104037, DOI: 10.1016/j.rineng.2025.104037.
61 Y. Chen, D. Ma, G. He and S. Pan, *Water*, 2024, **16**, 2389, DOI: 10.3390/w16172389.
62 A. Mills, R. H. Davies and D. Worsley, *Chem. Soc. Rev.*, 1993, **22**, 417–425, DOI: 10.1039/CS9932200417.
63 N. Basavaraj, A. Sekar and R. Yadav, *Mater. Adv.*, 2021, **2**, 7559–7582, DOI: 10.1039/d1ma00773d.
64 M. A. Al-Nuaim, A. A. Alwasiti and Z. Y. Shnain, *Chem. Pap.*, 2022, **77**, 677–701, DOI: 10.1007/s11696-022-02468-7.
65 A. Ajmal, I. Majeed, R. N. Malik, H. Idriss and M. A. Nadeem, *RSC Adv.*, 2014, **4**, 37003–37026, DOI: 10.1039/c4ra06658h.
66 A. Das, P. Ningthoukhongjam and R. G. Nair, *Water, Air, Soil Pollut.*, 2022, **233**, 282, DOI: 10.1007/s11270-022-05748-w.
67 A. Bouazza, S. Bassaid, A. Dehbi, N. Hadj-Zoubir, A. Alsalme and D. Robert, *React. Kinet., Mech. Catal.*, 2023, **1363**, 1625–1641, DOI: 10.1007/s11144-023-02429-5.
68 M. Saeed, M. Muneer, A. ul Haq and N. Akram, *Environ. Sci. Pollut. Res.*, 2022, **29**, 293–311, DOI: 10.1007/s11356-021-16389-7.
69 Y. Li, H. Zhang, D. Zhang, S. Yao, S. Dong, Q. Chen, F. Fan, H. Jia and M. Dong, *Molecules*, 2024, **29**, 1169, DOI: 10.3390/MOLECULES29051169.
70 M. Cai, M. Jin and L. K. Weavers, *Ultrason. Sonochem.*, 2011, **18**, 1068–1076, DOI: 10.1016/j.ultsonch.2011.03.010.
71 M. A. Meetani, M. A. Rauf, S. Hisaindee, A. Khaleel, A. Alzamly and A. Ahmad, *RSC Adv.*, 2011, **1**, 490–497, DOI: 10.1039/C1RA00177A.
72 X. Wu, M. Li, A. Abouserie, A. Frommelius, G. Dalfollo, T. Ohlerth and U. Simon, *Catal. Today*, 2024, **432**, 114620, DOI: 10.1016/J.CATTOD.2024.114620.
73 S. Kumar, S. T, B. Kumar, A. Baruah and V. Shanker, *J. Phys. Chem. C*, 2013, **117**, 26135–26143, DOI: 10.1021/jp409651g.

© 2026 The Author(s). Published by the Royal Society of Chemistry